NASA CR-193225

Semi-annual Report, January 15, 1994
Quarterly Report for July - December, 1993
Kendall L. Carder, University of South Florida
NASS-31716

a) Objectives:

The task of algorithm-development activities at USF continues. The algorithm for determining chlorophyll *a* concentration, [Chl *a*] and gelbstoff absorption coefficient for SeaWiFS and MODIS-N radiance data is our current priority.

b) Task Accomplished:

A preliminary algorithm for chlorophyll *a* and gelbstoff parameterized for the Gulf of Mexico in summer has been accomplished. The bio-optical algorithm being developed for SeaWiFS and MODIS-N is based on a semi-analytical model of remote-sensing reflectance (R_{rs}) and is an extension of the algorithm discussed in Carder et al. (1991). The major difference between the two occurs in the spectral term for the effects of backscattering and the upwelling distribution of radiance as developed in Lee et al. (1994). As a result of this change a bio-optical algorithm utilizing the SeaWiFS wavebands centered at 412, 443, 490, 555, and 670 nm is used to estimate chlorophyll *a* concentration ([Chl *a*]) and gelbstoff concentration, represented by its absorption coefficient at 400 nm ($a_g(400)$).

The R_{rs} model has numerous parameters that cannot be fixed and applied to the entire globe; i.e., they are site- and season-specific. For example, absorption per unit chlorophyll by phytoplankton can change with species, and with nutrient and lighting conditions by as much as a factor of five (Morel and Bricaud 1981; Carder et al. 1991; Morel et al. 1993). Also, particle size and concentration both have a significant effect on the spectral

(NASA-CR-193225) N94-23538
[ALGORITHM-DEVELOPMENT ACTIVITIES]
Quarterly Report, Jul. - Dec. 1993
(University of South Florida) 26 p Unclas

G3/51 0201708

backscattering coefficient, $b_b(\lambda)$, of ocean water, because pure water backscatters as $\sim \lambda^{-4}$, large particles backscatter as $\sim \lambda^{-0}$, and smaller diameter detritus and bacteria backscatter with a spectral dependence between the two (Morel and Ahn 1990, 1991). If many of these factors did not covary, the simple wavelength-ratio algorithms of the CZCS (Gordon and Morel 1983) would never have worked as well as they did. In trying to understand these covariances, we have developed semi-empirical expressions that depend on chlorophyll for some components of the model.

Extensive field data sets are needed to allow seamless modification of the model parameters with time and space. The changes required will be due mostly to changes in the dominant plankton groups present and the subsequent effects on bio-optical parameters such as pigment packaging. Acquiring such data sets on a global scale should be a major community goal during the next few years. We have developed a scenario that can both guide the parameterization process and provide an initial regional implementation of the algorithm.

Two cruises to the Gulf of Mexico were conducted, one during the spring and one during the summer of 1993, to acquire data for development and testing of the algorithm. Pigment data from the spring cruise are not yet available for model validation, but the optical and bio-optical portions of the algorithm have both been tested on the summer data, where [Chl *a*] ranged from < 0.10 to > 40 mg m^{-3}, and gelbstoff-to-phytoplankton absorption ratios at 443 nm ($a_g(443)/a_\phi(443)$) ranged from 0.3 to 3.0. Average errors for modeled versus measured data were 38% for [Chl *a*] and 37% for $a_g(400)$. The high-error values were associated with places in the Mississippi River plume where the absorption coefficient due to detritus and gelbstoff combined exceeded that for phytoplankton by as much as a

factor of five.

c) Data/Analysis/Interpretation:

c1): Data collection methods

The data used to develop and test the algorithm were collected during June 1993 on the COLOR cruise at stations shown in Fig. 1. The data taken include spectral remote-sensing reflectance ($R_{rs}(\lambda)$), chlorophyll *a* and pheopigment *a* concentrations ([Chl *a*] and [pheo *a*]), and spectral absorption coefficients for phytoplankton, detritus, and gelbstoff ($a_\phi(\lambda)$, $a_d(\lambda)$, and $a_g(\lambda)$).

$R_{rs}(\lambda)$ measurements:

$R_{rs}(\lambda)$ was measured from 390 to 1100 nm using a Spectron Engineering SE-590 hand-held spectrometer that was modified by adding a 200 μm slit and a vertical polarizer. The polarizer limits the Fresnel reflectance of skylight to values less than 2.1%, which is the minimum reflectance value for an unpolarized instrument (Jerlov 1968). This decreases uncertainties due to sea-surface waves in the instrumental field of view. An identically equipped SE-590 was used simultaneously without a polarizer to evaluate the polarization effects on $R_{rs}(\lambda)$. Spectral ratios of the polarized versus non-polarized data were within 3%, indicating that spectral effects due to polarization were not significant.

Three radiance spectra must be taken by the SE-590 in order to determine $R_{rs}(\lambda)$. These three measurements were taken rapidly in order and the process repeated twice to yield three sets of three radiance spectra at each station. First, a water-viewing measurement was

made at about 25° from nadir, typically at a 90° azimuthal angle from the solar plane. The second measurement was of the sky at a 25° zenith angle in the same azimuthal plane as the first measurement. The third measurement was of a horizontal Spectralon reflectance standard panel with a reflectance of about 10%. It is held by one scientist sighting on the horizon across the panel while a second scientist measures the reflected radiance at the same orientation as for the water-viewing measurement. The bi-directional reflectance distribution of the reflectance standard should be ascertained so that changes in illumination geometry can be corrected if necessary. If the panel is Lambertian, $\pi L_p(\lambda)/\rho(\lambda) = E_d(\lambda)$, where L_p is the measured panel radiance, $\rho(\lambda)$ is the irradiance reflectance of the panel, and E_d is the downwelling irradiance. If the panel is not Lambertian, the distribution function $Q_p(\Theta_0,\phi_0;\Theta,\phi) = \rho(\lambda)E_d(\lambda;\Theta_0,\phi_0)/L_p(\lambda;\Theta,\phi)$ for the panel should be used instead of π.

$R_{rs}(\lambda)$ is the ratio of upwelling water-leaving radiance to the downwelling irradiance incident upon the sea surface. It can be calculated from the three radiance measurements via

$$R_{rs}(\lambda) = \frac{\pi\,[N_w(\lambda) - r_f(\lambda)\,N_s(\lambda)]}{N_p(\lambda)} \qquad (1)$$

where $N_w = \sigma L_w$, $N_s = \sigma L_s$, and $N_p = \sigma L_p = \sigma\rho E_d/\pi$. N is digital counts, r_f is the Fresnel reflectance of the sea surface, L is measured radiance, σ is the responsivity of the SE-590 to radiance, and the subscripts 'w', 's', and 'p' refer to water, sky, and reflectance panel measurements. Note that this approach is not dependent on the instrumental calibration factor, σ, which divides out. It is only dependent upon the panel calibration factors, which remain stable unless the panel surface becomes contaminated.

pigment measurements:

[Chl *a*] and [pheo *a*] were determined fluorometrically on a Turner Designs 10-AU-005 fluorometer. The method used is described in Holm-Hansen and Reimann (1978), and it is an improvement of the method described in Strickland and Parsons (1972).

$a_\phi(\lambda)$ and $a_d(\lambda)$ measurements:

The absorption coefficients for particles and detritus, $a_p(\lambda)$ and $a_d(\lambda)$, were determined via the filter pad transmission technique (Mitchell and Kiefer 1988), and the methanol extraction technique (Kishino 1985; Roesler et al. 1989). The absorption coefficient for phytoplankton, $a_\phi(\lambda)$, is simply $a_p(\lambda) - a_d(\lambda)$.

$a_g(\lambda)$ measurements:

The absorption coefficient for gelbstoff, $a_g(\lambda)$, was measured at Hg-emission wavelengths (365, 404, 436, 546, and 578 nm) using a folded-path 1 m spectrophotometer. The regulated Hg arc source was evaluated for each sample measurement, using a calibrated reflectance target inserted in the optical path just in front of the sample chamber entrance window. The seawater sample was filtered immediately after collection using a 0.2 μm Gelman Supor 200 membrane filter, and was refrigerated until the end of the day, when all samples collected that day were run consecutively. A deionized water (DIW) blank was run before and after the group of samples. DIW and samples were introduced into the instrument by pumping through a 0.2 μm pore size Whatman Polycap 36AS cartridge filter. A Spectron Engineering SE-590 spectrometer was used as the sensor. Complete details of the $a_g(\lambda)$ measurement procedure will be presented at the AGU/ASLO Ocean Sciences

meeting in February, 1994.

c2): Algorithm Development

R_{rs} model:

The optical and bio-optical algorithms for SeaWiFS are based on an $R_{rs}(\lambda)$ model which is given by the following general equations (Lee et al. 1992; Lee et al. 1994):

$$R_{rs}(\lambda) = 0.176\frac{b_b(\lambda)}{Q(\lambda)a(\lambda)} \quad (2)$$

$$\frac{b_b(\lambda)}{Q(\lambda)} = \frac{b_{bw}(\lambda)}{Q_w(\lambda)} + \frac{b_{bp}(\lambda)}{Q_p(\lambda)} \quad (3)$$

$$\frac{b_{bp}(\lambda)}{Q_p(\lambda)} = X\left(\frac{400}{\lambda}\right)^Y \quad (4)$$

R_{rs} is remote-sensing reflectance, b_b is the total backscattering coefficient, Q is the upwelling irradiance-to-radiance ratio, E_u/L_u, a is the total absorption coefficient, and the subscripts 'w' and 'p' refer to water and particles. The lead coefficient 0.176 in Eq. 2 includes effects of the air-sea interface, $b_{bw}(\lambda)$ is known (Smith and Baker 1981), and the average value of $Q_w(\lambda)$ is 3.3 $ster^{-1}$ (Lee et al. 1992). $X = b_{bp}(400)/Q_p(400)$ and is an indication of the magnitude of $b_{bp}(\lambda)$, while Y provides its spectral shape. This Y term is especially important near river mouths where extremely fine clays and flocculates can remain after heavier particles have settled out of the sediment plume.

The behavior of X and Y will change with different water types, and we need to know *a priori* a means of classifying water types based simply on season, latitude, and $R_{rs}(\lambda)$. The two Gulf of Mexico data sets include hyper-spectral measurements of $R_{rs}(\lambda)$ and total absorption. X and Y were determined for each station by inverting the model expressed in Eqs. 2-4. Expressions were then sought for both X and Y as functions of R_{rs} at one or more of the SeaWiFS wavebands. It was found that X covaries with $R_{rs}(670)$, and linear regression on the summer data set yields $X = 0.0000328 + 3.485 \cdot R_{rs}(670)$ ($n=15$, $r^2=.95$; see Fig. 2). However, the 670 nm radiance band on SeaWiFS is likely to have too low a signal-to-noise ratio to be useful in clearer waters, and we restrict the use of this regression equation to waters where $R_{rs}(670) > 0.0008$. For clearer waters we use $X = b_{bp}(400)/Q_p(400)$ and $b_{bp}(400) = 0.0036 \cdot [\text{Chl } a]^{0.25}$, which is a function developed using the approach for estimating b_{bp} at other wavelengths found in Gordon et al. (1988). [Chl a] is estimated via a CZCS-type two-wavelength algorithm determined by linear regression of log[Chl *a*] vs. $\log[R_{rs}(443)/R_{rs}(555)]$ for the same data set, and $Q_p(400)$ is set to 4.0 $ster^{-1}$, which is an estimate based on near-surface upwelling irradiance and radiance data for the Gulf of Mexico provided by W. J. Rhea and C. Davis. Our equations for X for the Gulf of Mexico in the summer are summarized below.

$$\textit{for } R_{rs}(670) > 0.0008: \qquad X = 0.0000328 + 3.485\, R_{rs}(670) \tag{5}$$

$$\textit{for } R_{rs}(670) < 0.0008: \qquad X = 0.0036\, [Chl\ a]^{0.25}/4.0 \tag{6}$$

$$where \quad [Chl\ a] = 1.71\left(\frac{R_{rs}(443)}{R_{rs}(555)}\right)^{-1.99} \tag{7}$$

Y was found to covary with the spectral ratio $R_{rs}(443)/R_{rs}(490)$. Note that this ratio is not completely independent of absorption by phytoplankton and gelbstoff as both absorb more at 443 nm than at 490 nm. For offshore stations this ratio did provide the tightest correlation ($r^2 > 0.9$) with Y of any spectral ratio, and linear regression was used to estimate Y for these stations (Fig. 3). For more turbid waters near the river, however, it is expected that detritus and fine suspended sediments will produce a slightly blue-rich backscatter. We found that $a_d(412)$ covaried with $R_{rs}(670)$, and developed an expression for Y as a function of $R_{rs}(670)$. The equations used to calculate Y for the Gulf of Mexico in the summer are summarized below.

$$for \ \frac{R_{rs}(443)}{R_{rs}(490)} > 0.8: \quad Y = -2.7 + 3.75\,\frac{R_{rs}(443)}{R_{rs}(490)} \tag{8}$$

$$for \ \frac{R_{rs}(443)}{R_{rs}(490)} < 0.8: \quad Y = 0.3 + 30.0\,R_{rs}(670) \tag{9}$$

The inverse correlation of Y with [Chl *a*] implicit in Eq. 8 suggests that oligotrophic waters have smaller particles as has been discussed by others (Gordon and Morel 1983 and references cited). Also, the slope value of 3.75 in Eq. 8 was only slightly larger than that found for springtime, suggesting that summer backscattering is bluer than in the springtime, probably due to the presence of smaller phytoplankton and greater bacterial and detrital fractions in the summer.

Relationships such as these for X and Y are needed on a global basis for a truly mature global algorithm to evolve. We believe that sea-surface temperature (SST) can help with the parameterization since Y is expected to increase with reductions in nutrients or increases in SST.

Optical algorithm:

Using spectral ratios of $R_{rs}(\lambda)$ reduces the uncertainties in transmissivity through the air-sea interface that arise due to sea foam and wave-facet angles. Substituting Eqs. 3 and 4 into Eq. 2, rearranging, and forming a spectral ratio yields

$$\frac{R_{rs}(\lambda_i)}{R_{rs}(\lambda_j)} \frac{[b_{bw}(\lambda_j)/3.3 + X(400/\lambda_j)^Y]}{[b_{bw}(\lambda_i)/3.3 + X(400/\lambda_i)^Y]} = \frac{a(\lambda_j)}{a(\lambda_i)} \qquad \textbf{(10)}$$

At this point, the model is still strictly optical in nature (i.e., pigment concentration is not involved), and spectral ratios of total absorption coefficients can be determined from measurements of $R_{rs}(\lambda)$, given appropriate expressions for X and Y.

Bio-optical algorithm:

The bio-optical portion of the algorithm is derived by expanding the total absorption coefficient into its constituent parts:

$$a(\lambda) = a_w(\lambda) + a_\phi(\lambda) + a_d(\lambda) + a_g(\lambda) \qquad \textbf{(11)}$$

The subscripts 'w', 'ϕ', 'd', and 'g' represent components due to water, phytoplankton, detritus, and gelbstoff. If we can develop expressions for $a_\phi(\lambda)$, $a_d(\lambda)$, and $a_g(\lambda)$ as functions only of [Chl *a*] and $a_g(400)$, then we can combine Eqs. 10 and 11 and use three wavelength bands to get a system of two equations in two unknowns.

The phytoplankton term can be written $a_\phi(\lambda) = a^*_\phi(\lambda)$[Chl *a*], where $a^*_\phi(\lambda)$ is the chlorophyll *a*-specific absorption coefficient for phytoplankton. An empirical relationship between nutrient availability (which correlates with chlorophyll concentration) and cell size (which affects pigment packaging) seems to hold for much of the ocean (Herbland et al. 1985; Carder et al. 1986), and its effect on $a^*_\phi(\lambda)$ has been suggested (Carder et al. 1991) to have the form

$$a^*_\phi(\lambda) = a_0(\lambda) \exp\left[a_1(\lambda) \tanh\left[a_2(\lambda) \ln(a_3(\lambda)\,[Chl\,a])\right]\right] \quad \textbf{(12)}$$

The equation parameters $a_0(\lambda)$ - $a_3(\lambda)$ can be determined for a given region and season from measured $a^*_\phi(\lambda)$ and [Chl *a*] data. $a_0(\lambda)$ is the most important of these parameters, as it is directly proportional to $a^*_\phi(\lambda)$. For simplicity, only $a_0(\lambda)$ and $a_1(\lambda)$ were used to parameterize $a^*_\phi(\lambda)$, with $a_2(\lambda)$ and $a_3(\lambda)$ held constant. Fig. 4 shows the measured data and the modeled curve for λ = 443 nm for the summer cruise, and the parameters for all wavelengths are listed in Table 1. The summer $a_0(\lambda)$ values shown are about twice the spring values, most likely due to smaller cells, less [Chl *a*] needed per cell due to higher light, and more photo-protective pigments required in the summer.

$a_d(\lambda)$ and $a_g(\lambda)$ can both be fit to a curve of the form $a_x(\lambda) = a_x(400) \exp(-S_x(\lambda\text{-}400))$

where the subscript 'x' refers to either 'd' or 'g' (Roesler et al. 1989; Carder et al. 1991). Due to this similarity in spectral shape, we eliminate the $a_d(\lambda)$ term and allow both detrital and gelbstoff absorption to be represented by $a_g(\lambda)$. For the summer data set, which had many stations near the Mississippi River plume, average values of 0.011 nm^{-1} and 0.017 nm^{-1} were determined for S_d and S_g, respectively, and we use an intermediate spectral slope value of 0.015 nm^{-1} for the combined slope parameter, S. The combined detritus and gelbstoff absorption term is thus written

$$a_g(\lambda) = a_g(400)\, e^{-0.015(\lambda - 400)} \qquad \textbf{(13)}$$

The model equations used in the bio-optical algorithm are derived by inserting Eqs. 12 and 13 into Eq. 11 and substituting the result into both the numerator and denominator of Eq. 10. The left hand side of the resulting equation is determined completely by $R_{rs}(\lambda)$ inputs, so two of these equations are needed to solve for both [Chl *a*] and $a_g(400)$. Based on the shapes of the absorption curves for chlorophyll and gelbstoff, equations using the spectral ratios 412/443 and 443/555 should provide the best separation of the two. Signal-to-noise considerations may make it necessary to switch to other bands, but the philosophy behind the algorithm will remain the same. Using the spectral ratios suggested above yields the following equations:

$$\frac{R_{rs}(412)}{R_{rs}(443)}\frac{[b_{bw}(443)/3.3 + X(400/443)^{Y}]}{[b_{bw}(412)/3.3 + X(400/412)^{Y}]} = \frac{a_w(443) + a_\phi^*(443)[Chl\,a] + a_g(400)\,e^{-0.015(443-400)}}{a_w(412) + a_\phi^*(412)[Chl\,a] + a_g(400)\,e^{-0.015(412-400)}} \quad (14)$$

$$\frac{R_{rs}(443)}{R_{rs}(555)}\frac{[b_{bw}(555)/3.3 + X(400/555)^{Y}]}{[b_{bw}(443)/3.3 + X(400/443)^{Y}]} = \frac{a_w(555) + a_\phi^*(555)[Chl\,a] + a_g(400)\,e^{-0.015(555-400)}}{a_w(443) + a_\phi^*(443)[Chl\,a] + a_g(400)\,e^{-0.015(443-400)}} \quad (15)$$

These equations are solved via look-up tables (LUTs). First, fifty-element arrays are created for both [Chl *a*] and $a_g(400)$. The right hand sides of Eqs. 14 and 15 are then solved for each combination of [Chl *a*] and $a_g(400)$ array values, and the resulting pairs of total absorption ratios, a(443)/a(412) and a(555)/a(443), are tabulated in a 2-dimensional array (i.e., the LUT). The left hand sides of the equations are evaluated for each input spectrum of measured $R_{rs}(\lambda)$, yielding modeled total absorption ratios. The LUT is then searched for absorption ratios which are just above and just below the modeled values. Modeled [Chl *a*] and $a_g(400)$ values are then calculated by interpolating between the LUT values of [Chl *a*] and $a_g(400)$ that correspond to the LUT absorption ratios determined in the previous step. This process can be visualized in Fig. 5 which depicts the LUT as a nomogram of absorption ratios, along with the input data points for the summer data set.

d): Discussion

The optical portion of the summer algorithm was tested against measured total absorption coefficients. Fig. 6a shows the algorithm results versus measured values for a(443)/a(412), while those for a(555)/a(443) are shown in Fig. 6b. The algorithm resulted in average errors of 7.6% and 11.5%, respectively. These low errors are not surprising, since the X and Y parameters used were determined in part from the measured total absorption coefficients.

The bio-optical portion of the summer algorithm was tested against measured values of [Chl *a*] (Fig. 7a) and measured $a_g(400)$ (Fig. 7b). This algorithm resulted in average errors of 37.9% and 36.6%, respectively.

The accuracy of estimates of [Chl *a*] can be limited by many factors, especially at high concentrations. Such factors include low signal-to-noise of the measured radiance, high absorption by detritus or suspended sediment poorly predicted variations in $a^*_\phi(\lambda)$, S, and high patchiness in the river plumes.

Errors resulting from low signal-to-noise in L_w cannot be easily corrected. Such pixels must be flagged and the data processed with an alternate algorithm using wavelengths with a stronger signal. Such algorithms will lack the spectral finesse to as accurately separate gelbstoff from pigments, so an accuracy flag should be attached to such pixels.

Errors resulting from excessive detritus or suspended sediments can occur near river mouths and other coastal areas. For example, some of the summer cruise stations in the Mississippi River plume had $a_d(412)$ values larger than 0.4 m^{-1}, which was often larger than $a_\phi(412)$ and nearly as large as $a_g(412)$. This has significant ramifications at 555 nm since detrital absorption at that wavelength can be as large or larger than gelbstoff or water

absorption. In the future, $a_d(\lambda)$ and $a_g(\lambda)$ should be treated separately in such areas. As a preliminary investigation, we found that $a_d(412)$ correlated well with $R_{rs}(670)$, and if $a_d(412)$ can be determined from $R_{rs}(670)$, a_d at other wavelengths can be calculated via $a_d(\lambda) = a_d(412) \exp(-0.011(\lambda-412))$. This type of correction will be implemented in the next version of the algorithm. Its implementation will, however, require a three-dimensional LUT which will increase processing time, so it should only be used in regions with well defined detritus problems.

Unpredictable variations in $a^*_\phi(\lambda)$ affect [Chl *a*] retrievals directly since $a^*_\phi(\lambda)$ is a measure of light absorption per unit [Chl *a*], and these variations can be caused by many factors. Revisiting Fig. 4, note the scatter of the measured $a^*_\phi(443)$ values at the high [Chl *a*] end. The largest deviations of the measured values from the modeled line tend to occur at stations where $a_d(412) > a_\phi(412)$. Some of the variation is likely also due to non-monotonic transitions between dinoflagellate- and diatom-dominated phytoplankton assemblages with increasing [Chl *a*]. This is so because the modeled $a^*_\phi(\lambda)$ curve is expected to be consistent with a smooth, monotonic transition. In addition, light adaptation by phytoplankton can effect their pigment packaging and, consequently, $a^*_\phi(\lambda)$. In fact, this problem appears to be the limiting factor in improving algorithm accuracy, at least for these waters in the summer.

e): Future Actions

There may be some hope, however, when dealing with changes in $a^*_\phi(\lambda)$ that are associated with nutrient enrichment due to upwelling or vertical mixing. The empirical problem is knowing exactly when and how much to vary $a_0(\lambda)$ and other parameters of Table

1 to blend the model seamlessly from one season and geographical location to another. Species succession and pigment packaging are influenced to a large extent by the nutrients available (e.g. no silica means no diatoms), and a satellite-based means of estimating nutrient availability would provide a cue for transitioning parameters such as $a_0(\lambda)$ on a seasonal or geographic basis.

Satellite-derived sea-surface temperature (SST) may provide such a means. Increases in SST can indicate increased stability, reduced mixing across the thermocline, and reduced nutrients. Decreases in SST can indicate upwelling and/or overturn of the upper layer, reduced stability, and increased nutrients. A model relating SST to nutrient (N, P, Si) availability on a global basis has been developed using the NODC nutrient, sigma-t and temperature data base (Kamykowski and Zentara 1986; Kamykowski 1987). When SST exceeds a critical value for a given region of the ocean, a specific nutrient is predicted to be limited. Given this model, a species reliant on an influx of the limited nutrients from across the nutricline can be expected to be succeeded by phytoplankton ensembles more reliant on other nutrients or upon recycled nutrients. Nutrient-availability estimates, not surprisingly, would also play a key role in improving the accuracy of primary-production models (Kamykowski 1987; Gregg and Walsh 1992).

A temperature-coupled bio-optical model will identify regions of strong SST anomalies and provide a means to make first-order adjustments to the algorithm should that be desirable for future versions of the algorithm. Such algorithms require SST measurements from AVHRR, which is beyond the scope of our present task for developing algorithms for SeaWiFS. We do hope, however, that collaboration with D. Kamykowski will help in the initial global parameterization of the model and its seasonal transition from one state to

another.

f): References cited

Carder, K.L., R.G. Steward, J.H. Paul, and G.A. Vargo, Relationships between chlorophyll and ocean color constituents as they affect remote-sensing reflectance models, *Limnol. Oceanogr.*, 31, 403-413, 1986.

Carder, K.L., S.K. Hawes, K.A. Baker, R.C. Smith, R.G. Steward, and B.G. Mitchell, Reflectance Model for Quantifying Chlorophyll *a* in the Presence of Productivity Degradation Products, *J. Geophys. Res.*, 96(C11), 20,599-20,611, 1991.

Gordon, H.R., O.B. Brown, R.H. Evans, J.W. Brown, R.C. Smith, K.S. Baker, and D.K. Clark, A semi-analytic model of ocean color, *J. Geophys. Res.*, 93, 10,909-10,924, 1988.

Gordon, H.R., and A.Y. Morel, Remote assessment of ocean color for interpretation of satellite visible imagery: A review, *Springer*, 1983.

Gregg, W. and J. Walsh, Simulation of the 1979 spring bloom in the Mid-Atlantic Bight: A coupled physical/biological/optical model, *J. Geophys. Res., Vol. 97*, 5723-5743, 1992.

Herbland, A., A. Le Bouteiller, and R. Raimbault, Size structure of phytoplankton biomass in the equatorial Atlantic Ocean, *Deep Sea Res.*, 32, 819-836, 1985.

Holm-Hansen, O., and B. Riemann, Chlorophyll *a* determination: Improvements in methodology, *Oikos*, 30, 438-448, 1978.

Jerlov, N.G., Factors influencing the transparency of the Baltic waters, *Medd. Oceanogr. Inst. Goteborg*, 25, 1955.

Kamykowski, D. and S. Zentara, Predicting plant nutrient concentrations from temperature and sigma-t in the upper kilometer of the world ocean, *Deep-Sea Res. 33*, 89-105, 1986.

Kamykowski, D., A preliminary biophysical model of the relationship between temperature and plant nutrients in the upper ocean, *Deep-Sea Res. 34*, 1067-1079, 1987.

Kishino, M., M. Takahashi, N. Okami, and S. Ichimura, Estimation of the spectral absorption coefficients of phytoplankton in the sea, *Bull. Mar. Sci.*, 37, 634-642, 1985.

Lee Z., K.L. Carder, S.K. Hawes, R.G. Steward, T.G. Peacock, and C.O. Davis, An interpretation of high spectral resolution remote-sensing reflectance, in *Ocean Optics XI*, Proc. SPIE 1705, 1992.

Lee Z., K.L. Carder, S.K. Hawes, R.G. Steward, T.G. Peacock, and C.O. Davis, A model for interpretation of hyper-spectral remote-sensing reflectance, submitted to *Appl. Opt.*

Mitchell, B.G., and D.A. Kiefer, Variability in pigment specific particulate fluorescence and absorption spectra in the northeastern Pacific Ocean, *Deep Sea Res.*, 35, 665-689, 1988.

Morel, A.Y., and Y.H. Ahn, Optical efficiency factors of free-living marine bacteria: Influence of bacterioplankton upon the optical properties and particulate organic carbon in oceanic waters, *J. Marine Res.*, 48, 145-175, 1990.

Morel, A.Y., and Y.H. Ahn, Optics of heterotrophic nanoflagellates and ciliates: A tentative assessment of their scattering role in oceanic waters compared to those of bacterial and algal cells, *J. Marine Res.*, 49, 177-202, 1991.

Morel, A.Y., Y.H. Ahn, F. Partensky, D. Vaulot, and H. Claustre, *Prochlorococcus* and *Synechococcus*: A comparative study of their optical properties in relation to their size

and pigmentation, *J. Marine Res.*, 51, 617-649, 1993.

Morel, A.Y, and A. Bricaud, Theoretical results concerning light absorption in a discrete medium and application to the specific absorption of phytoplankton, *Deep Sea Res.*, 28, 1357-1393, 1981.

Roesler, C.S., M.J. Perry, and K.L. Carder, Modeling *in situ* phytoplankton absorption from total absorption spectra in productive inland marine waters, *Limnol. Oceanogr.*, 34, 1510-1523, 1989.

Smith, R.C., and K.S. Baker, Optical properties of the clearest natural waters (200-800 nm), *Appl. Opt.*, 20, 177-184, 1981.

Strickland, J.D.H., and T.R. Parsons, A practical handbook of seawater analysis, Fish. Res. Board Can. Bull. 167, 2nd ed., 310pp., 1972.

g:) Published and submitted manuscripts:

1. Lee, Z., K. L. Carder, S. K. Hawes, R. Steward, T. Peacock and C. O. Davis, A model for Interpretation of Hyperspectral Remote-sensing Reflectance, submitted to *Appl. Opt.*

2. Carder, L. K., P. Reinersman, and R.F. Chen, AVIRIS Calibration Using the Cloud-Shadow Method, *Proceeding of the 4th JPL AVIRIS Workshop*, Oct., 1993.

Table 1. Parameters for the $a^*_\phi(\lambda)$ vs. [Chl *a*] relationship (Eq. 12) for data taken on the COLOR cruise, June 1993. Only the 412, 443, and 555 nm parameters are used in the algorithm described in this paper.

wavelength	a_0	a_1	a_2	a_3
412	0.040	0.95	-0.5	1.0
443	0.060	0.90	-0.5	1.0
490	0.039	0.81	-0.5	1.0
510	0.026	0.60	-0.5	1.0
555	0.008	0.75	-0.5	1.0

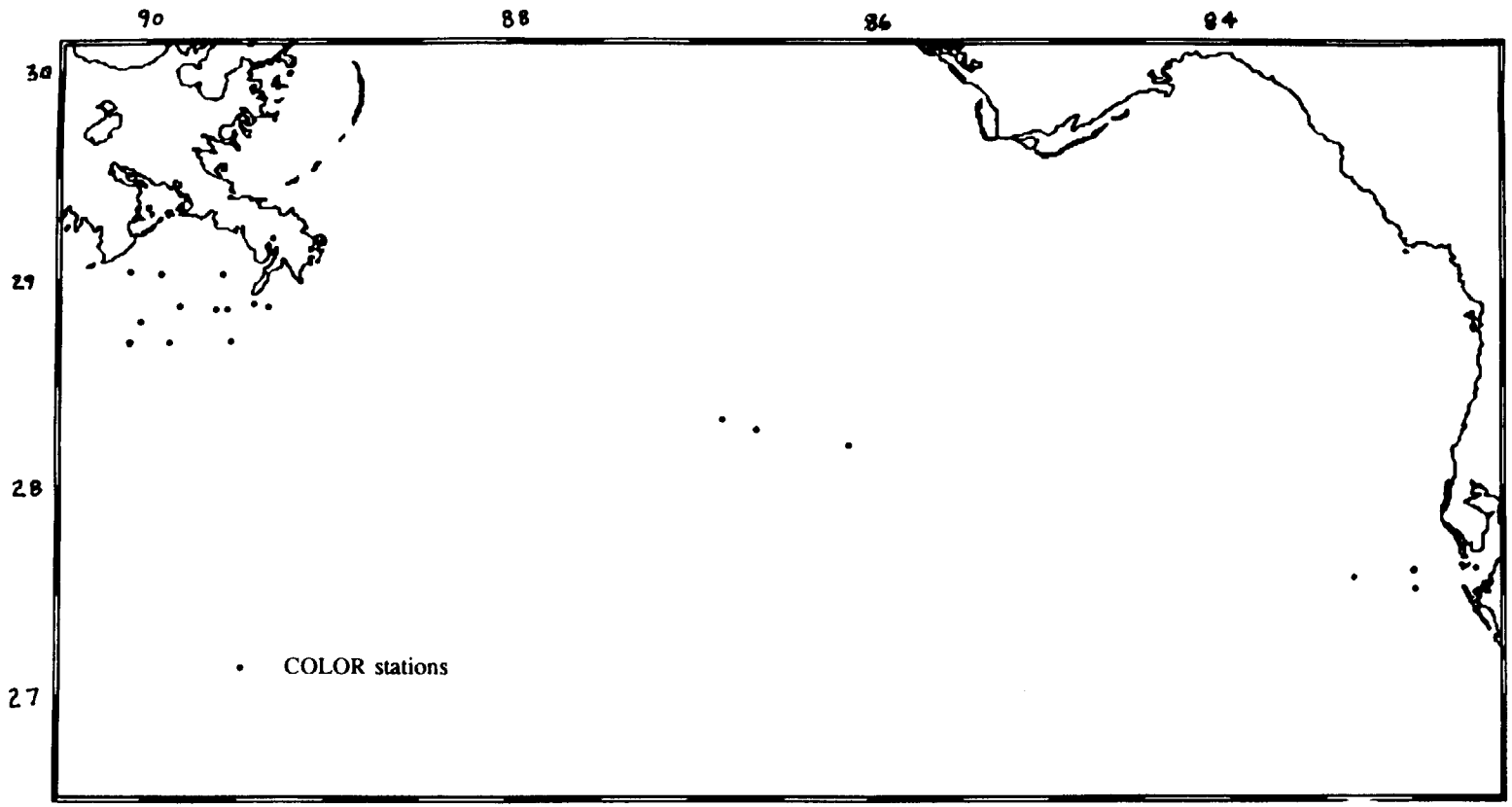

Fig. 1. Station locations for the COLOR cruise, June 1993.

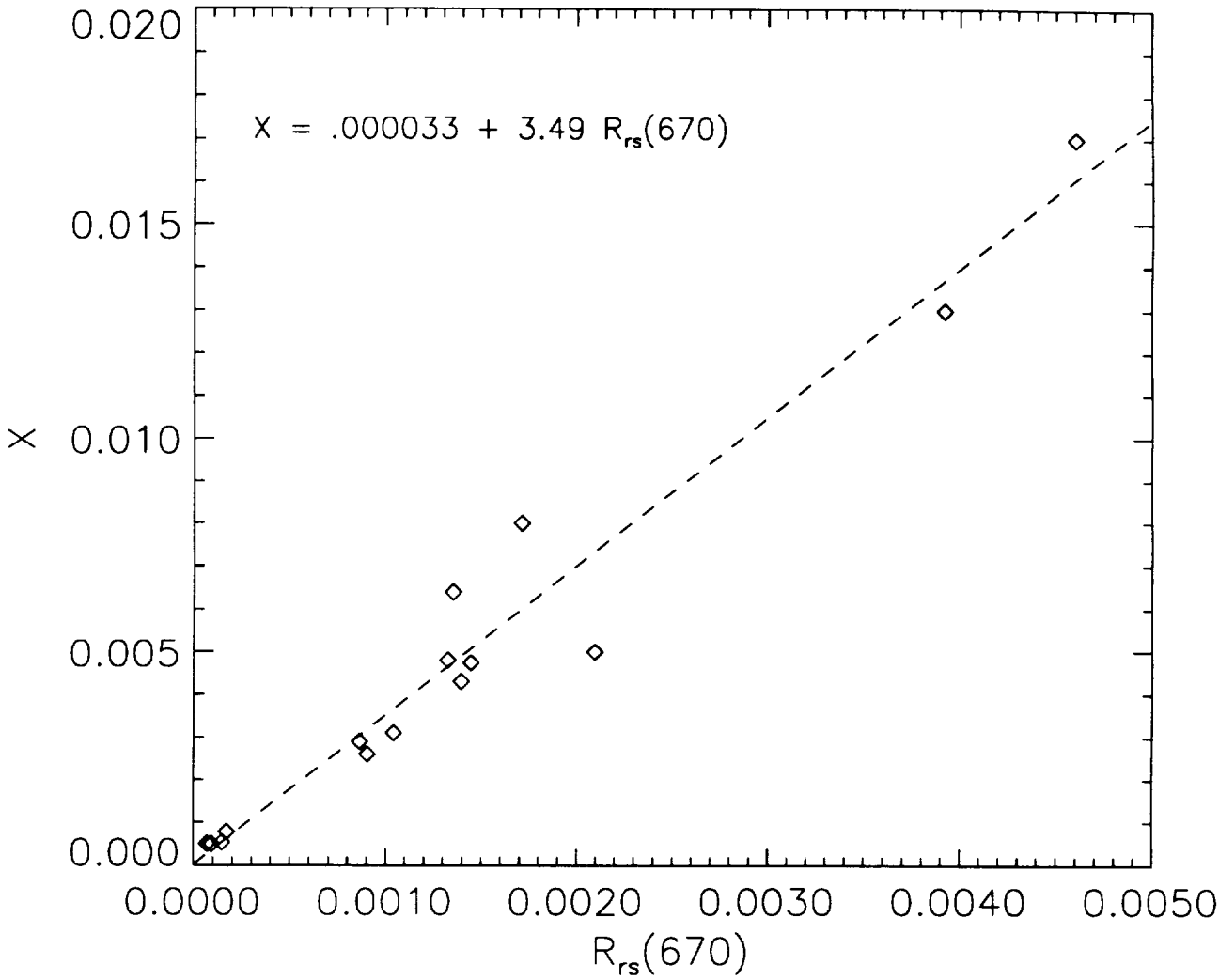

Fig. 2. X vs. $R_{rs}(670)$ regression ($n=16$, $r^2=0.95$).

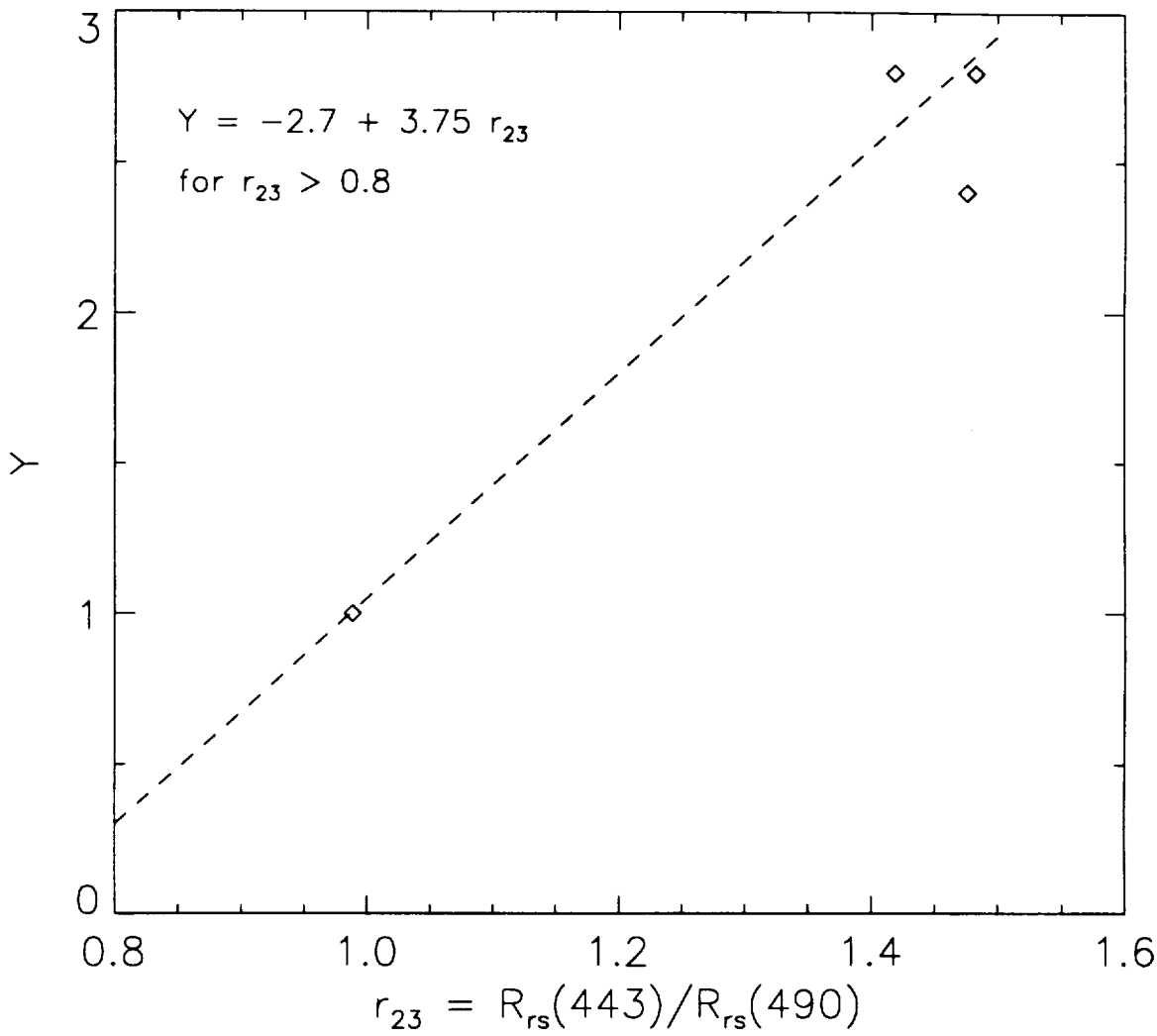

Fig. 3. Y vs. r_{23} (=$R_{rs}(443)/R_{rs}(490)$). Only points where $r_{23} > 0.8$ (i.e. low [Chl *a*] points) are considered.

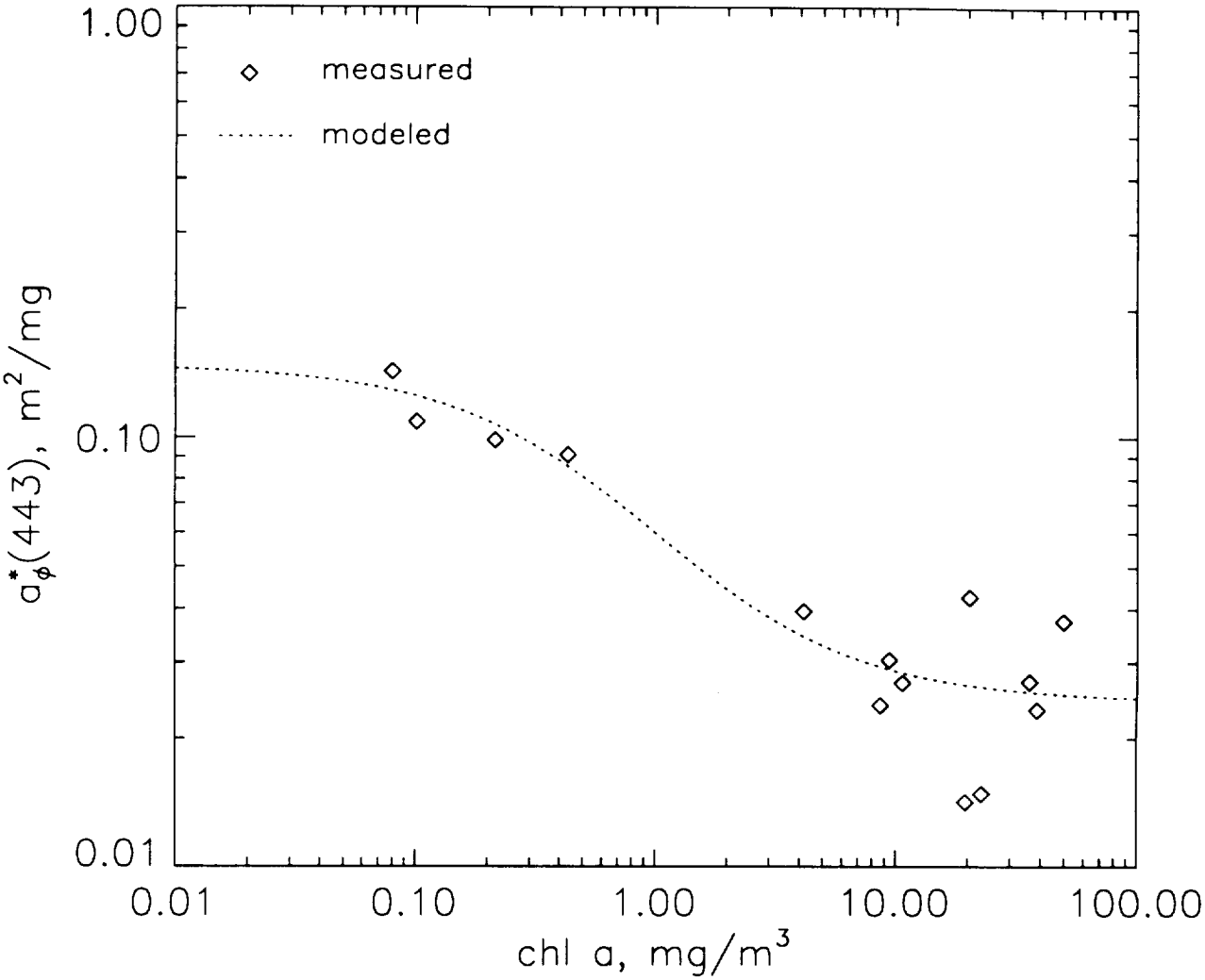

Fig. 4. $a^*_\phi(443)$ vs. [Chl *a*]. The dotted line is determined by the parameters in Table 1 and Eq. 12.

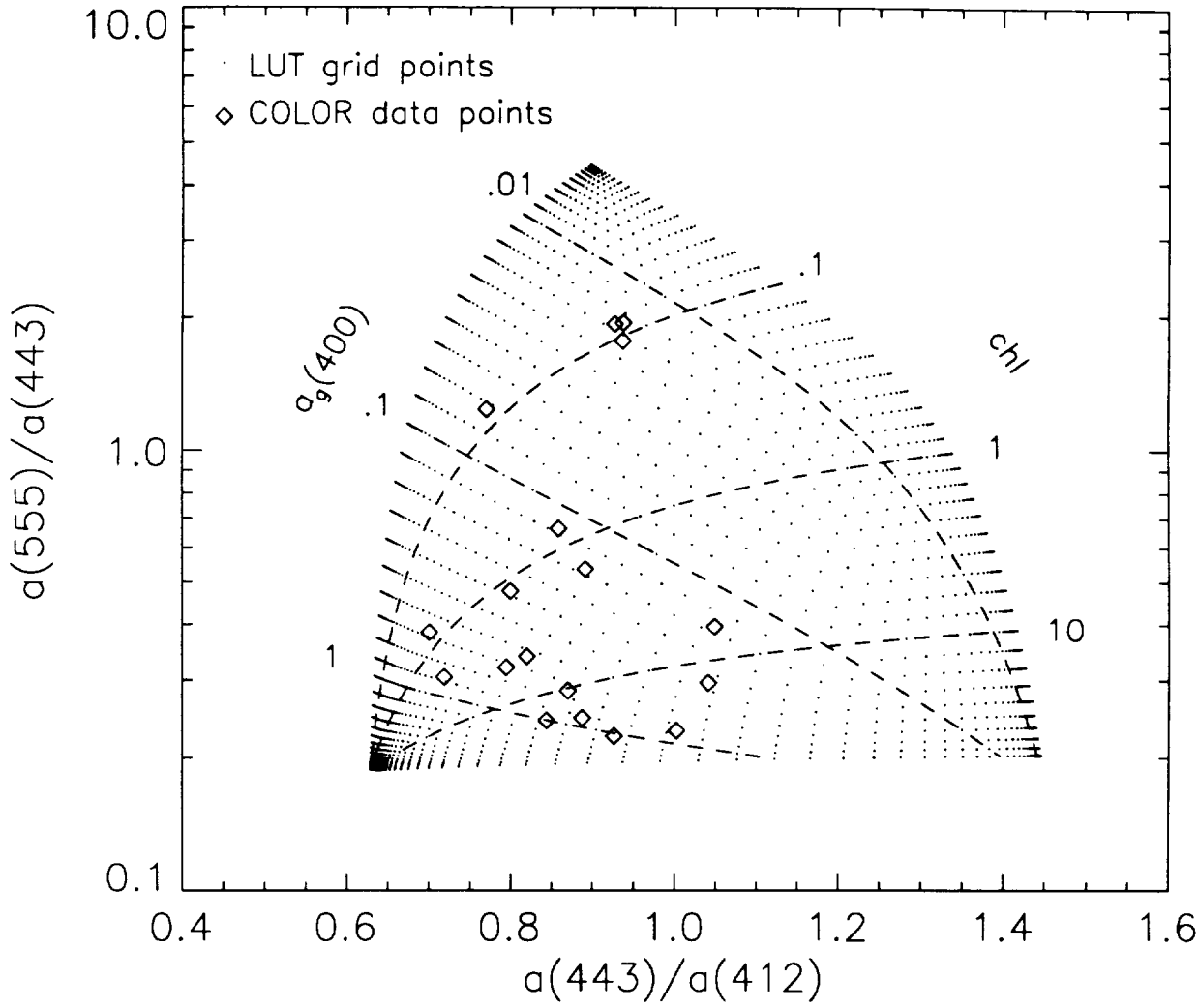

Fig. 5. Nomogram depicting the look-up table (LUT) of absorption ratios (dots) and the input absorption ratios (diamonds) calculated from R_{rs} data. The dotted lines connect LUT absorption ratios that correspond to constant [Chl *a*] or $a_g(400)$. [Chl *a*] and $a_g(400)$ are calculated from the input absorption ratios via bi-linear interpolation of the input points between the four LUT grid points that surround it.

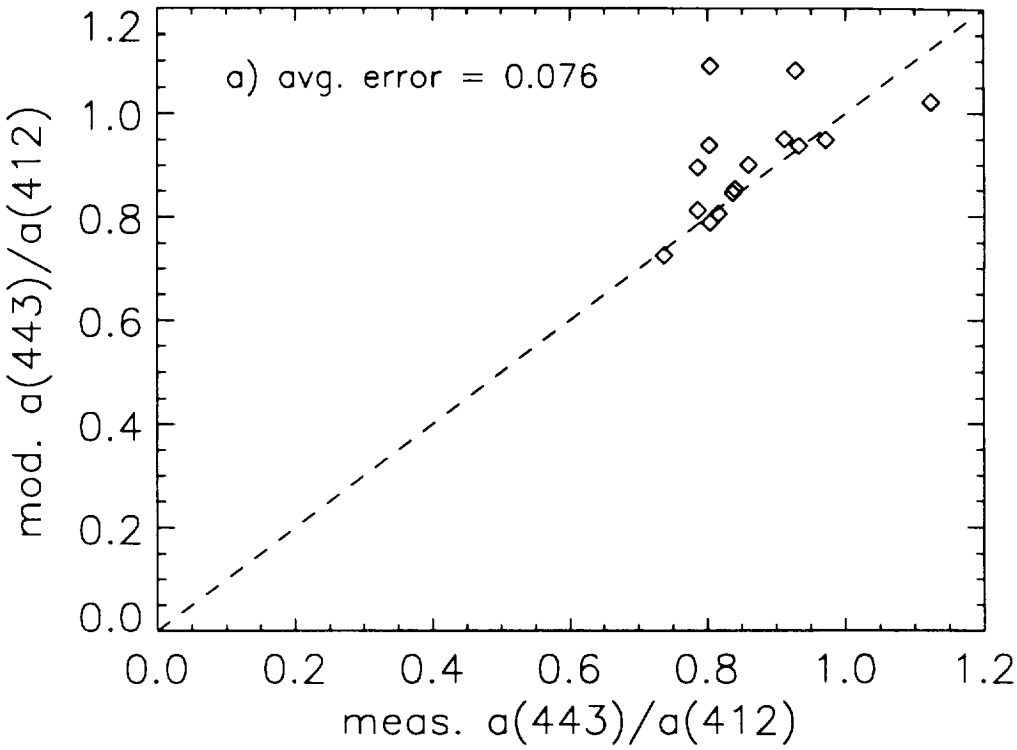

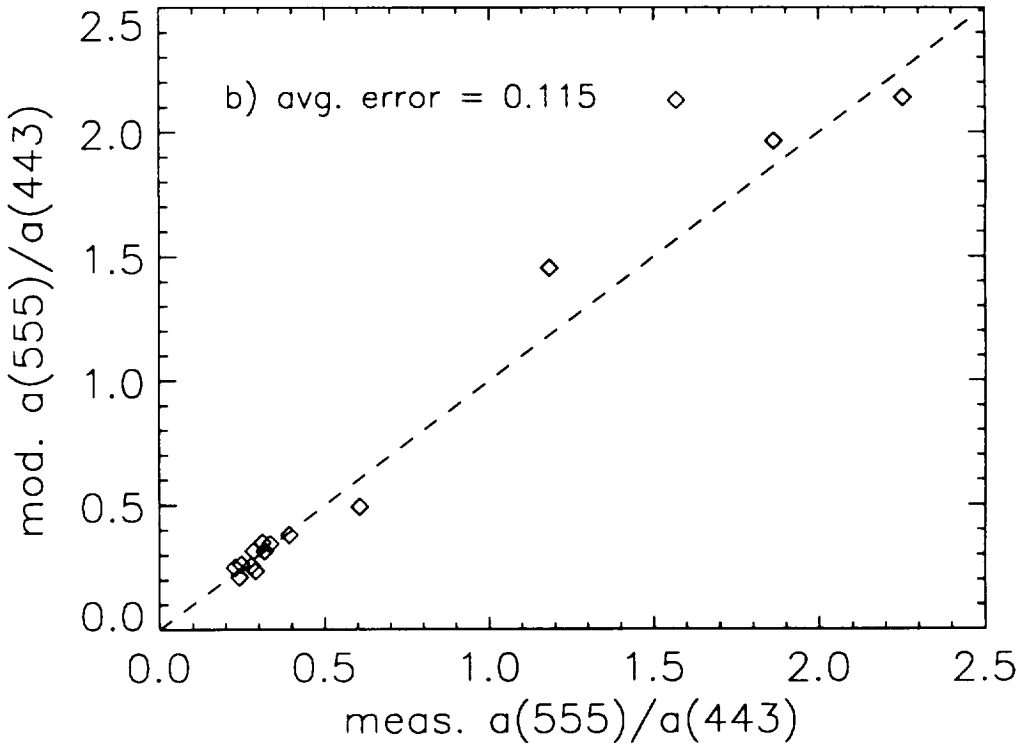

Fig. 6. Optical algorithm results. Measured vs. modeled absorption ratios for a) a(443)/a(412), and b) a(555)/a(443).

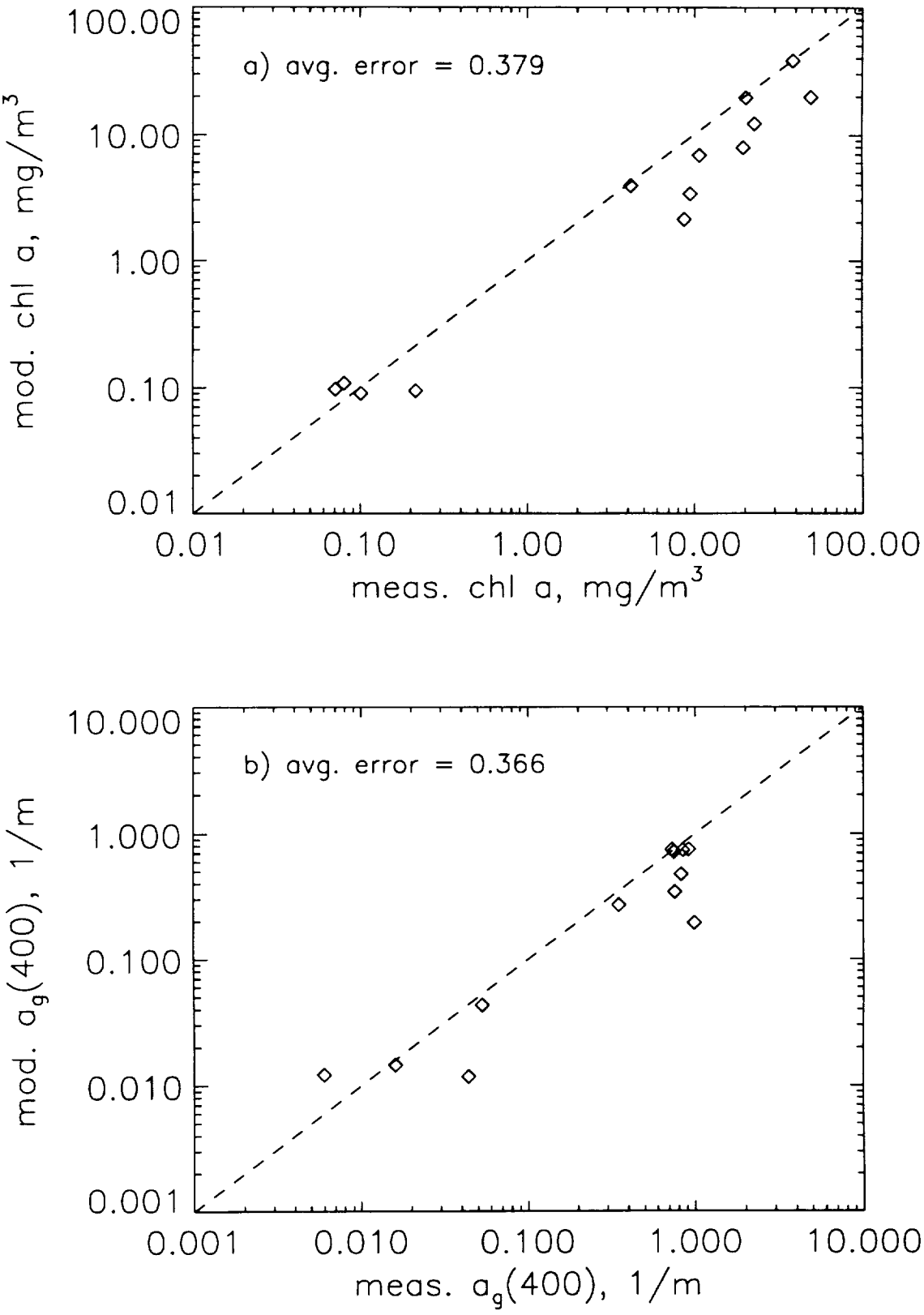

Fig. 7. Bio-optical algorithm results. Measured vs. modeled values for a) [Chl *a*], and b) $a_g(400)$.